ACS APPLIED MATERIALS & INTERFACES
Research Article
www.acsami.org

Tunable Photoluminescent Core/Shell Cu^+-Doped ZnSe/ZnS Quantum Dots Codoped with Al^{3+}, Ga^{3+}, or In^{3+}

Jason K. Cooper,[†,‡] Sheraz Gul,[†,§] Sarah A. Lindley,[†] Junko Yano,[§] and Jin Z. Zhang*[,†]

[†]Department of Chemistry and Biochemistry, University of California, Santa Cruz, California 95064, United States
[‡]Materials Science Division, Lawrence Berkeley National Laboratory, Berkeley, California 94720, United States
[§]Physical Biosciences Division, Lawrence Berkeley National Laboratory, Berkeley, California 94720, United States

Supporting Information

ABSTRACT: Semiconductor quantum dots (QDs) with stable, oxidation resistant, and tunable photoluminescence (PL) are highly desired for various applications including solid-state lighting and biological labeling. However, many current systems for visible light emission involve the use of toxic Cd. Here, we report the synthesis and characterization of a series of codoped core/shell ZnSe/ZnS QDs with tunable PL maxima spanning 430−570 nm (average full width at half-maximum of 80 nm) and broad emission extending to 700 nm, through the use of Cu^+ as the primary dopant and trivalent cations (Al^{3+}, Ga^{3+}, and In^{3+}) as codopants. Furthermore, we developed a unique thiol-based bidentate ligand that significantly improved PL intensity, long-term stability, and resilience to postsynthetic processing. Through comprehensive experimental and computational studies based on steady-state and time-resolved spectroscopy, electron microscopy, and density functional theory (DFT), we show that the tunable PL of this system is the result of energy level modification to donor and/or acceptor recombination pathways. By incorporating these findings with local structure information obtained from extended X-ray absorption fine structure (EXAFS) studies, we generate a complete energetic model accounting for the photophysical processes in these unique QDs. With the understanding of optical, structural, and electronic properties we gain in this study, this successful codoping strategy may be applied to other QD or related systems to tune the optical properties of semiconductors while maintaining low toxicity.

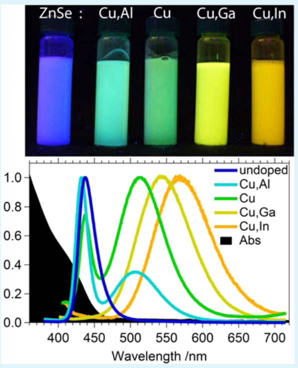

KEYWORDS: *doped, ZnSe, quantum dot, passivation, lifetime, QD-LED, shell*

1. INTRODUCTION

Semiconductor quantum dots (QDs) have been the subject of great interest in the past few decades as light emitting materials in a number of technologically important applications including solid-state lighting and biological labeling[1] due to their unique electronic and optical properties which can be tuned by changing their size/shape[2−5] or by doping with other elements.[6−8] In these systems, stability, uniformity, tunability, efficiency, and toxicity are important considerations. Currently, CdSe-based QDs are being developed in academia and industry as next generation solid-state lighting materials[9] due to their tunable and uniform green and red emission which arises from quantum confinement of the low bulk bandgap (1.74 eV). As such, these phosphors may be coupled to a blue emitter, such as GaN or InGaN, to achieve fluorescence down conversion and white light emission[10,11] or used in electroluminescent devices.[12−18] However, the efficiency of a mixture of QDs for white light generation would be limited by overlap of component QD absorption and photoluminescence (PL) spectra or self-absorption from a small Stokes shift and broad PL features.[11,19,20] Furthermore, Cd pollution accumulates in waste streams, and its toxicity poses serious concerns to the environment and human health.[21]

Promising alternatives to the CdSe system are doped, wide-bandgap semiconductor QDs, such as zinc chalcogenides doped with Cu, Mn, Eu, or Ga,[7,22,23] which exhibit minimal self-absorption due to a large Stokes shift and boast reduced environmental impact. Broad spectral coverage is achievable in these II−VI semiconductor systems as doping introduces electronic states into the bandgap,[24−26] allowing photogenerated carriers to relax into donor or acceptor states where they can recombine with their counterparts remaining at or near the band edges. Many such approaches have been reviewed by Wu and Yan.[27] For instance, introduction of Cu as a dopant in ZnSe QDs creates an acceptor level that shifts the fluorescence from blue to green (λ_{max} = 430−530 nm).[22] However, if the dopant atoms possess different oxidation states from the host lattice atoms, single element doping can create charge imbalance that leads to compensating defects such as vacancies and/or lattice distortion. In a previous report, we determined that Cu dopes the ZnSe lattice as a +1 ion,[28] causing a compensating defect consisting of a second Cu^+ and a

Received: April 1, 2015
Accepted: April 20, 2015
Published: April 20, 2015

DOI: 10.1021/acsami.5b02860
ACS Appl. Mater. Interfaces 2015, 7, 10055−10066

selenium vacancy (V_{Se}).[29] These V_{Se} defects have been identified in both ZnSe and ZnS.[29,30]

To avoid these defects, the charge imbalance may instead be relieved through codoping. Codopants are usually of ionic radius similar to that of the host lattice and of opposite charge to the primary dopant. As such, the dopant and codopant together replace a cation and anion of the host semiconductor.[31,32] Alternatively, a neutral lattice with no vacancies may instead be achieved by replacing a second Zn^{2+} with a trivalent cation codopant.[33] In previous work, we observed that using an Al^{3+} codopant enhanced the resultant PL yield through elimination of V_{Se} by compensating the charge imbalance, while preserving the emission spectrum.[28] We have provided a review of these approaches in a recently published perspective.[34]

In the present work, we extend this codoping strategy and utilize the codopant to impart donor states into the bandgap which, in conjunction with the Cu acceptor states, offer an additional mechanism to red shift the PL through donor−acceptor pair (DAP) recombination. We demonstrate that combining the Cu^+ primary dopant with Al^{3+}, Ga^{3+}, or In^{3+} codopants can shift the PL of ZnSe/ZnS QDs from blue to orange, covering a broad range of visible region of the spectrum (λ_{max} = 430−570 nm). A large full width at half-maximum (fwhm) of 80 nm, on average, enables broad spectral coverage which extends out to 700 nm in the Cu,In doped system, which is advantageous for white light generation. Additionally, we achieve long-term stability, robustness to postsynthetic processing, and inhibited oxidative damage through incorporation of a bidentate ligand. Furthermore, we elucidate the fundamental photophysical processes responsible for this tunable emission and correlate the energetics to the local structure surrounding the primary dopant and codopant atoms using a combination of powerful experimental and computational techniques.

2. EXPERIMENTAL DETAILS

2.1. ZnSe/ZnS, ZnSe:Cu/ZnS, and ZnSe:Cu,D/ZnS QD Synthesis. The synthesis of ZnSe, ZnSe:Cu, and ZnSe:Cu,D used herein was an adaptation from Gul et al.[28] Specifics may be found in the Supporting Information (SI) Supplementary Methods along with a description of the ZnS shell addition.

2.2. Capping Ligand Synthesis. The capping ligand was freshly synthesized alongside each QD synthesis. In a N_2 glovebox, a solution was prepared containing 0.1469 g of lipoic acid, 0.2639 g of trioctylphosphine (TOP), and 0.1907 g of oleylamine. The mixture was placed in a 25 mL three neck round-bottom flask connected to a Schlenk line and degassed for 10 min with 3 pump/purge cycles with dry N_2. While stirring, the reaction was heated to 120 °C and maintained for the totality of the QD synthesis (∼16 h). During the reaction between lipoic acid and oleylamine, H_2O is released which can react with TOP and cause it to become oxidized, thus providing electrons to cleave the disulfide bond. Indeed, the reaction color changed from yellow to clear, indicating bond cleavage. The resultant reaction mixture was added directly to the crude ZnSe:Cu,D/ZnS pot where the thiol termination of the ligand engages a strong bidentate interaction with the QD surface at both Zn and S sites.

2.3. HRTEM/STEM-EELS. TEM investigation was carried out using an FEI F20 UT Tecnai HRTEM/STEM microscope operated at 200 kV accelerating voltage, located at the National Center for Electron Microscopy (NCEM) at Lawrence Berkeley National Laboratory. This microscope is equipped with a postcolumn energy filter (GIF Tridiem from Gatan) and an EELS detector for analytical characterization.

2.4. Steady State Spectroscopic Characterization. The room temperature optical absorption spectrum of the QDs dispersed in dichloromethane (DCM) was recorded with a Hewlett-Packard 8452A diode array spectrometer. The room temperature PL spectrum was recorded using a PerkinElmer luminescence spectrometer on the purified samples dispersed in DCM. Temperature-dependent PL measurements were collected on a custom built system at 20−330 K through control by a closed cycle liquid helium cryostat (Janus Research Co., Wilmington, MA, USA). The purified, solid phase samples were placed between two quartz windows and were excited with a 405 nm continuous wave laser (100 mW Excelsior, Spectra-Physics, Santa Clara, CA, USA) after passing the laser through a 405 nm notch filter and attenuating the beam to 14 μW. The spot size at the sample was 0.3 mm in diameter. The sample luminescence was collected at 90° with respect to the excitation, was filtered through a 407 nm long-pass filter, and was incident on an Andor Shamrock spectrometer equipped with a 600 lines/mm grating blazed at 500 nm (Andor Technology Ltd., Belfast, U.K.). The light was recorded with an Andor iDus 410 CCD operated at −90 °C. Wavelength calibration was done with a Hg calibration lamp, and the CCD and grating efficiency was corrected for using a NIST traceable quartz tungsten halogen 45 W light source with a known spectral profile.

2.5. Time-Resolved Photoluminescence. Time-resolved PL was measured with time-correlated single photon counting (TCSPC) at room temperature on purified samples dispersed in DCM using a system and techniques described elsewhere.[28,35] Briefly, a 200 MHz Ti:sapphire laser (tunable 790−820 nm) with an output of 350 mW was passed through a Conoptics pulse picker to select a 500 kHz pulse train and a BiBO crystal to generate the second harmonic. This ∼405 nm centered, 4 μJ, laser was used to excite the sample. The fluorescence light from the sample was collected tangentially to the excitation laser and separated with a monochromator. Detection was achieved with an ID100 avalanche photodiode (IDQ, Switzerland). The instrument response function was 50 ps, as determined from scattering of the excitation light from a nondairy creamer solution. Data were analyzed with IGOR Pro (wavemetrics) as well as singular value decomposition global fitting procedures developed in-house for Matlab.

2.6. Density Functional Theory Calculations. Calculations on ZnSe, ZnSe:Cu, ZnSe:Cu,Al, ZnSe:Cu,Ga, and ZnSe:Cu,In were performed with the PWscf package contained in the Quantum ESPRESSO code.[36] Density function theory (DFT) calculations were performed with the PBE functional and ultrasoft pseudopotentials on a supercell containing 64 atoms for ZnSe, ZnSe:Cu,Al, ZnSe:Cu,Ga, and ZnSe:Cu,In and 63 atoms for ZnSe:Cu. The optimized unit cell parameter (a) was 5.74 Å. For ionic position optimization, damp dynamics were used with a $4 \times 4 \times 4$ K point mesh. The Cu−Se bond distances were constrained to the experimentally determined bond distances from EXAFS, as PBE was not able to duplicate the experimental lattice position of Cu, while the remaining atoms were allowed to vary. SCF and NSCF calculations were performed with kinetic energy cutoff of 70 Ry for wave functions and 700 Ry for the charge density, a $8 \times 8 \times 8$ K point mesh, and tetrahedral occupations. The local density of states (LDOS) were calculated with projwfc.x.

2.7. EXAFS. X-ray absorption measurements at the Cu, Zn, and In *K*-edges were performed at the Stanford Synchrotron Radiation Lightsource (SSRL), on beamline 7-3 at 10 K on purified, solid phase samples. The monochromatized radiation from a Si (220) double crystal monochromator was detuned to 50% of its maximum at the metal *K*-edge to minimize the effects of higher harmonics. The beam size on the sample was reduced to 0.5 mm vertical and 1.0 mm horizontal fwhm. In the case of In *K*-edge, intensity of the incident X-rays (I_0) was monitored by an Ar-filled ion chamber in front of the sample, whereas N_2 was used for other measurements. Along with the samples, respective metal foils were measured during each scan using a reference ion chamber to calibrate the energy scale. Zn data were collected in transmission mode, while Cu and In measurements were carried out in fluorescence mode using a 30 element Ge detector (Canberra). QD samples were deposited in Plexiglas sample holders with Kapton film windows.

All data were processed using standard programs based on IFEFFIT.[37,38] After calibrating the energy, individual scans were averaged together to improve the signal-to-noise ratio. Athena software was used for background removal and extraction of EXAFS oscillations

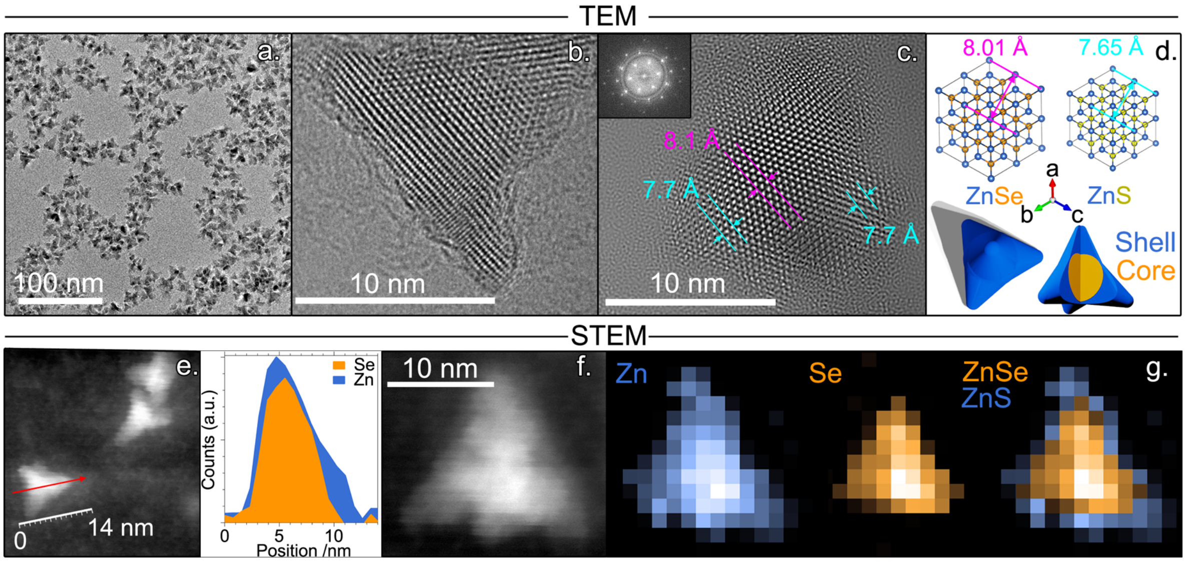

Figure 1. TEM and STEM analysis of ZnSe/ZnS core/shell QDs. (a) Low resolution TEM indicates that the particle dimensions are on the order of 12 nm and tetrapodal in shape. (b) High resolution TEM of a single particle shows the high degree of crystallinity. (c) An inverse Fourier transform (FT) image of the inset FT diffraction spots illustrates that the core is composed of ZB-ZnSe with lattice spacing of 8.1 Å, whereas the shell material is composed of ZB-ZnS with lattice spacing of 7.7 Å. (d) For reference, the crystal structures of ZB-ZnSe and ZB-ZnS are shown as well as representative 3D models of the core/shell, tetrapod QDs. (e) STEM images confirm the overall tetrapodal structure, and the line scan spanning 14 nm from base to tip shows that Se is isolated to the QD core whereas Zn is contained throughout. (f/g) Drift-corrected EELS mapping of the particle shown in f confirms that Se is confined to the core, supporting the assertion that the core is composed of ZnSe and the shell is composed of ZnS.

Scheme 1. Reaction Mechanism for the Synthesis of the Custom Capping Ligand

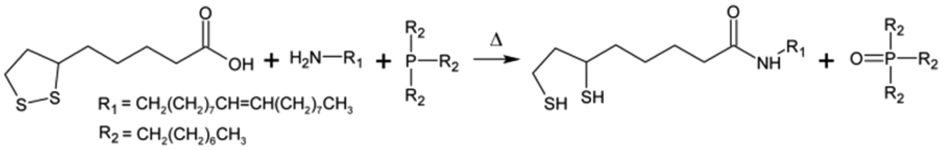

$\chi(k)$ as a function of photoelectron wavenumber k. The extracted k-space data, $k^3\chi(k)$, was then used to Fourier transform the data into r-space. Theoretical EXAFS models were calculated using FEFF6[39] and fitting program Artemis was used for fitting the data.

3. RESULTS AND DISCUSSION

3.1. Surface Passivation, Structure, and Morphology. In order to address the common issues of low PL yield and long-term instability, we developed a two-pronged approach to passivate surface dangling bonds. First, a ZnS shell was added to insulate both the electron and the hole and confine them to the ZnSe core. A similar approach taken by Jana et al. improved the PL stability of aqueous soluble ZnSe:Cu QDs by passivating Se-rich surfaces through introduction of a S shell which improves oxidation resistance.[40] After shell addition, transmission electron microscopy (TEM) reveals the resultant tetrapodal shape and high monodispersity (Figure 1a). The tetrapods extend ~12 nm from base to tip and are single crystalline in nature (Figure 1b). Furthermore, the inverse Fourier transform (FT) of a high resolution TEM image of a single QD reveals lattice spacing measurements that support the core/shell structure (Figure 1c). The spacing of 8.1 Å in the core region and 7.7 Å in the shell region correspond well with those expected for the zinc blende (ZB) crystal structures of ZnSe and ZnS, respectively (Figure 1d). Three-dimensional (3D) models of the core/shell tetrapods are shown as visualization aids (bottom of Figure 1d). The QD structure was also studied by scanning TEM (STEM) where the tetrapodal shape is more apparent (Figure 1e). To corroborate the assignments gleaned from lattice spacing measurements, the elemental composition was collected as a function of position across one arm of a tetrapod by combining STEM with electron energy loss spectroscopy (EELS) (Figure 1e). The scan spanned 14 nm in the base to tip direction indicated by the red arrow. Zn is found throughout the length of the particle whereas Se is confined to the core region; a sulfur signal could not be isolated from the large carbon-related background signal. We further confirmed this spatial assignment through elemental mapping of an entire particle (Figure 1f/g). The EELS spectrum at two points, representing the core and shell regions, is provided in SI Figure S1. These analyses support that the core is composed of ZnSe (~8 nm) while the shell is composed of ZnS (~2 nm).

3.2. Improved Photoluminescence Yield and Stability with Custom Designed Capping Ligand. Complete confinement is not always realized after shell addition as tunneling and Fermi level alignment may allow the photoelectron to travel into the shell where it is again susceptible to surface trapping from dangling bonds.[41,42] As such, we designed and incorporated a custom bidentate, thiol-based capping ligand as a second measure to ensure complete electronic surface passivation. It should be noted that using surfactants and ligands that bind weakly with the impurity atoms is a prerequisite for doping, as strongly bound ligands hinder the adsorption and subsequent doping of the impurity atoms.[8,43,44] However, typical postsynthetic processing, including cleaning of ZnSe QDs from the crude reaction mixture, can be quite challenging and often results in complete quenching of the PL due to the loss of the weakly bound capping ligand or oxidation.[40] Therefore, the weak binding octadecylamine ligand was used initially to ensure efficient doping of the core, but exchanged with our strong binding thiol-based ligand after doping in order to fortify the QDs against typical cleaning conditions. We synthesized the new ligand by modifying lipoic acid, the procedure for which is shown in Scheme 1. Lipoic acid is often used in aqueous synthesis methods or in ligand exchange to improve water solubility. Since water solubility was not desired here, the acidic functional group of lipoic acid was instead used to attach oleylamine and create a hydrophobic backbone. This approach was also pursued in order to improve intermolecular ligand stabilization through backbone hydrogen bonding of neighboring ligands by way of the amide bond.

The PL of the QDs at each stage of modification is compared in Figure 2 for two representative samples, ZnSe:Cu,Al/ZnS (Cu,Al) (Figure 2a) and ZnSe:Cu,Ga/ZnS (Cu,Ga) (Figure 2b). The samples were prepared at the same optical density at the wavelength of excitation, 380 nm (3.26 eV). Prior to shell addition, both samples displayed relatively low PL and emission could barely be detected by the naked eye. Also, very weak host emission could be seen for ZnSe:Cu,Al. After the ZnS shell was added, the PL for both samples was seen to slightly improve. Addition of the bidentate capping ligand resulted in more complete surface passivation of the dangling bonds and a 10-fold improvement in integrated PL intensity. This effect suggests that the ZnS shell alone was an incomplete insulator for the ZnSe core when considering the photoexcited electron. Alternatively, it could indicate incomplete coverage of the ZnSe core by the ZnS shell. Either way, after the capping ligand addition, dangling bonds at the ZnS surface and any remaining ZnSe surfaces were more completely passivated, resulting in reduced surface trapping and a dramatic improvement in PL yield. As desired, the ZnSe/ZnS system retained excellent PL even after being washed several times, crashed, stored, and resuspended in chloroform.

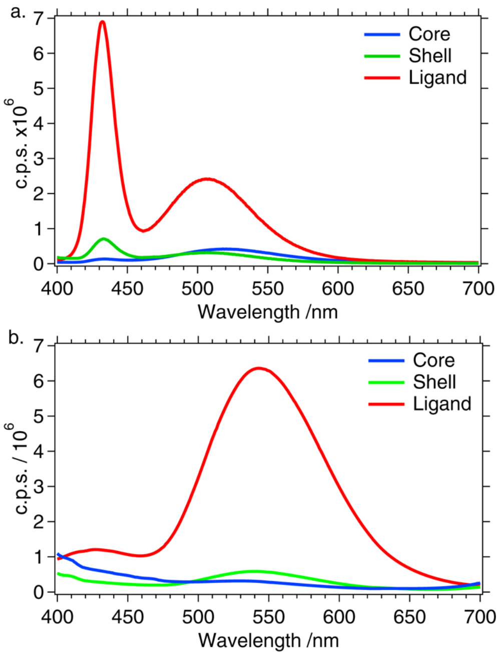

Figure 2. Representative PL spectra of (a) ZnSe:Cu,Al and (b) ZnSe:Cu,Ga QDs dispersed in chloroform before growth of the ZnS shell (core), after the ZnS shell growth (shell), and after the addition of the ligand (ligand). Excitation wavelength: 380 nm.

For long-term storage, the QDs were dispersed in DCM and stored in a freezer. The PL collected on the Cu,Al and Cu,Ga samples after storing for 600 and 620 days show a 4× and 5× reduction in integrated PL intensity, respectively, as compared to 0 days (the day of synthesis; SI Figure S2). No shift in the PL position or line shape was observed in either sample indicating the long-term stability of the emission profile. Overall, the increased PL yield and robustness of the resultant product as a result of the ZnS shell and ligand addition represent significant achievements in ZnSe QD synthesis, which is important for practical applications of such QDs.

It is clear from these results that adequate surface passivation is not only important for yield and stability but also critical for observing emission processes that may otherwise be suppressed by surface trapping or other nonradiative recombination processes.[45] For instance, the host-related band edge PL (440 nm) in the Cu,Al system was not seen in our previous report[28] and is also not seen for the bare ZnSe:Cu,Al core shown in Figure 2a. However, host-related emission becomes increasingly apparent after the addition of the ZnS shell and even more pronounced with the combination of shell and ligand. Band-edge PL is allowed so long as the valence band (VB) photogenerated hole and the conduction band (CB) electron are not trapped by the surface, making this recombination much more sensitive to surface quality. As such, competing pathways such as surface trapping may serve to reduce the host emission disproportionally compared to the Cu-related emission. The Cu-related emission in this system occurs through recombination of the CB electron to the hole bound to the Cu donor state. Strong localization at the Cu acceptor provides stabilization of the Cu-related recombination mechanism even with surface trapping of the photohole present in the core sample. For this reason, Cu-related emission is seen for all stages of the synthesis. It should be noted that, for the Cu,Ga sample, very little host emission was observed at any stage of the reaction. Further details regarding the emission mechanism which describe this observation are provided later. Briefly, it is due to localization of the photoelectron at a Ga-related acceptor state. The combination of hole and electron localization at Cu and Ga centers diminishes the host-related PL. The PL intensity, however, is still affected due to lost flux of photogenerated species toward nonradiative pathways at the surface.

3.3. Optical Properties of the Codoped Quantum Dots.

To assess the extent of tunability and possible self-absorption, the optical properties were investigated with UV–vis absorption and PL spectroscopies. The UV–vis spectra of undoped ZnSe/ZnS (undoped), singly doped ZnSe:Cu/ZnS (Cu), and codoped ZnSe:Cu,Al/ZnS (Cu,Al), ZnSe:Cu,Ga/ZnS (Cu,Ga), and ZnSe:Cu,In/ZnS (Cu,In) core/shell QDs are shown in Figure 3a and are vertically offset for clarity. No change in absorption was observed with the inclusion of the primary dopant (Cu^+) or codopants (Al^{3+}, Ga^{3+}, or In^{3+}); the absorption onsets of all the samples occurred at the same energy, 2.97 eV (417 nm), demonstrating the high degree of uniformity of the core size from batch to batch. The Gaussian fit of the first exciton absorption band, which applies to all of

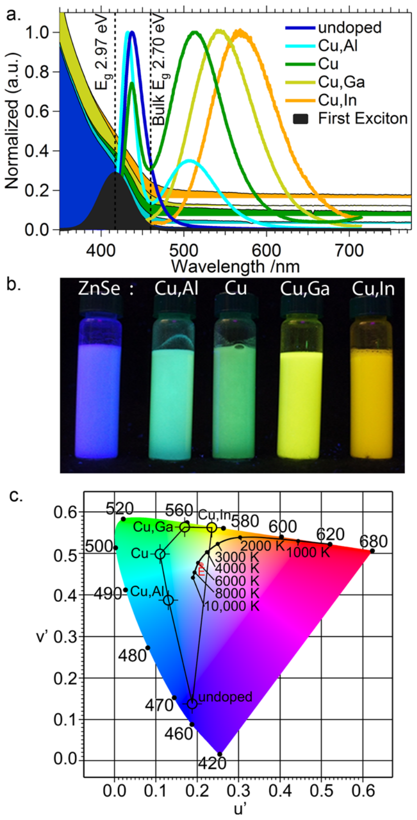

Figure 3. (a) Normalized absorption and PL spectra (λ_{ex} = 380 nm) of undoped ZnSe/ZnS (undoped), ZnSe:Cu,Al/ZnS (Cu,Al), ZnSe:Cu/ZnS (Cu), ZnSe:Cu,Ga/ZnS (Cu,Ga), and ZnSe:Cu,In/ZnS (Cu,In). Absorption spectra are shown as filled curves, and PL spectra are shown as solid lines. Absorption spectra are offset for clarity. E_g and bulk E_g represent the absorption onset of the ZnSe/ZnS QDs and bandgap of bulk ZnSe, respectively. Samples are dispersed in chloroform. Excitation wavelength for photoluminescence: 380 nm. (b) Photograph of the codoped ZnSe/ZnS QD system as excited by UV light. (c) CIE 1976 chromaticity plot showing the PL spectra from panel a mapped onto the u′,v′ color space. Also indicated is the equal-energy radiator 'E'. Panels a and b were reproduced, in part, with permission from ref 34. Copyright 2014 American Chemical Society.

the samples studied, is also indicated for clarity. Considering the Bohr exciton radius of bulk ZnSe is 4.5 nm,[46,47] the optical properties of the these QDs are expected to be affected by quantum confinement. Indeed, the absorption onsets (indicated as E_g) are blue-shifted from that of bulk ZnSe (indicated as bulk E_g), which has a bandgap of 2.70 eV (460 nm) at room temperature.[46,48] Zinc blende-ZnS has a bulk bandgap of 3.68 eV (337 nm), and, as such, no contribution from the ZnS shell could be resolved for the samples in the spectral region studied.

The corresponding PL spectra are shown as solid lines in Figure 3a. The spectra were transformed to photon flux vs photon energy using eq 1, where $I_0(\lambda)$ is PL intensity as a function of wavelength, and subsequently fit with multi-Gaussian fitting, as shown in SI Figure 3.[49] The average fwhm is 80 nm for the doped samples. The relative integrated area of the spectral components is also provided.

$$I_0(\lambda)\ \mathrm{d}\lambda = \frac{\lambda^2 I_0}{1240\ \mathrm{eV{\cdot}nm}}\ \mathrm{d}E \tag{1}$$

The undoped sample has a prominent band edge emission in the blue, centered at 437 nm. After incorporation of Cu^+ into the ZnSe core, a new emission peak in the green is observed at 517 nm, along with residual host (ZnSe) band edge emission at 436 nm. Introducing Al^{3+} as a codopant results in a green emission band centered at 509 nm but increased host emission at 432 nm. We attribute the increased host emission to decreased charge-compensating defect formation (i.e., V_{Se}), which acts to red shift the PL in the singly doped system. With a Ga^{3+} codopant, the PL was shifted significantly to the red and resulted in very clean yellow emission by eye, centered at 550 nm. The host emission observed in the previous samples was completely eliminated. Finally, In codoping resulted in the largest red shift of all the samples, with PL centered at 570 nm, which also showed no evidence of host-related emission. A photograph of the samples as illuminated by UV light illustrates the blue to orange PL span of this ZnSe system (Figure 3b). It should be noted that the absorption and PL regions are significantly distinct due to the large Stokes shift, allowing the ZnSe/ZnS QD system to avoid efficiency losses due to self-absorption. Experiments were conducted to include a Tl^{3+} codopant to further red shift PL to ~635 nm (SI Figure S4), but its incorporation into the host lattice was severely limited by its relatively large size, resulting in incomplete doping and poor overall PL uniformity.

Using the CIE (International Commission on Illumination) 1976 chromaticity coordinates, the combination of the undoped and Cu,In QDs could generate white light with an approximately 4,000 K color temperature, as shown in Figure 3c. For reference, incandescent light is 2,800 K, halogen light is 3,000 K, and direct sunlight is 4,800 K. However, mixtures of the QDs reported herein could achieve cooler white light color temperatures; decreasing the quantum confinement in the Cu,In system is expected to red shift the PL and lower the potential color temperature further. Therefore, these QDs are promising for application in next generation white light QD-LED technologies.

3.4. Reduced Trap State Emission with Codoping and Quantum Yield Determination.

The effect of codoping on the PL of the QDs were examined through the temperature dependence of the PL from 18 to 330 K using a 405 nm (3.06 eV) CW excitation light source at 10−15 mW cm^{-2}. This temperature study reveals the existence of significant defect-related PL in the undoped, Cu-doped, and Cu,In-doped systems. The temperature dependence of the undoped ZnSe/ZnS QD PL is shown in Figure 4a, and those for the remaining samples are presented in SI Figure S5. The primary defect emission is observed at 535 nm (2.32 eV) with a sideband at approximately 650 nm (1.9 eV). The defect features decay monotonically with increasing temperature. The bandedge emission red shifts with increasing temperature, consistent with thermal activation of lattice phonons.[50] The exact nature of the defect emission is beyond the scope of this study and requires further investigation in the future. Here, we use it to qualitatively assess the quality of the QDs in terms of PL properties.

The temperature dependence of the integrated PL spectrum for all five samples is shown in Figure 4b, and the Arrhenius plot is shown in SI Figure S6. Additionally, for the undoped sample, the bandedge (E_g) and defect-related PL integrated from 400 to 475 nm and from 475 to 800 nm, respectively, are also shown. Here, the defect-related PL exhibits a strong sigmoidal thermal quenching response between 70 and 160 K, whereas the bandedge PL has a more modest and linear dependence on temperature starting with a QY of 38% at 20 K

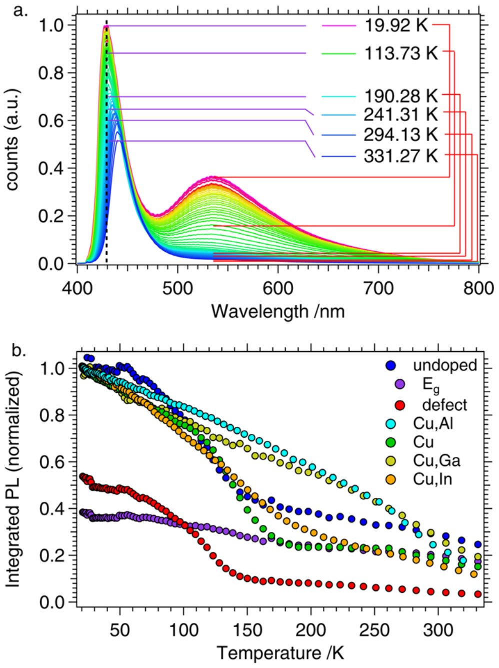

Figure 4. (a) Temperature-dependent PL of the ZnSe/ZnS QDs, in solid powder form, with relative counts indicated by horizontal lines and color coded to relate to either band edge (E_g), purple, or defect emission, red. The vertical black broken line indicates the band edge emission position (429 nm) at 19.92 K. (b) Temperature-dependent PL quenching of ZnSe/ZnS (undoped), ZnSe:Cu/ZnS (Cu), ZnSe:Cu,Al/ZnS (Cu,Al), ZnSe:Cu,Ga/ZnS (Cu,Ga), and ZnSe:Cu,In/ZnS (Cu,In) QDs. Also shown are the E_g (400−490 nm) and defect (490−800 nm) integrated areas of the undoped sample. Additional temperature-dependent spectra are shown in SI Figure S5.

and decreasing to 17% at 330 K. This effect is observed in the undoped, Cu-doped, and Cu,In codoped samples. However, the Cu,Al and Cu,Ga samples do not exhibit the same drop in integrated PL intensity in this temperature range. The absence of these defect-related PL in the Cu,Al and Cu,Ga samples suggests that codoping with Al or Ga helps to eliminate intrinsic defect trapping/emission in Cu-doped ZnSe.

Measurements of the fluorescence quantum yield (QY) can be challenging due to a number of factors. Furthermore, considering the system under study is not a simple two-level system, but rather involves multiple recombination pathways, we focus on the external quantum efficiency (EQE). In an attempt to estimate the EQE of these QDs, we have employed two methods to provide a lower and upper limit. The first method was through comparison of the PL intensity and optical density of the QDs to that of perylene dye (with known QY = 0.87, in ethanol).[51] By this method, the QY of the samples were 10 ± 5%. However, this method did not provide the precision necessary to discriminate between the samples.

For the second method, we place an upper bound on the EQE by considering the low temperature (18 K) PL intensity to have unity EQE. Alternatively stated, we take the low temperature PL intensity to be the maximum possible PL achievable in the current system in the absence of phonon assisted nonradiative recombination. A similar approach has been taken by Chang-Hasnain to examine InP micropillars.[52] At room temperature, the EQE is observed to be as follows: undoped (30%) = Cu,Ga (30%) > Cu,Al (25%) > Cu (20%) = Cu,In (20%). From this perspective, the optimal codopant in this system is therefore Ga^{3+}, which we attribute to its ideal size compared to the host lattice and lack of defect formation as the Ga^{3+} charge balances that of Cu^+. For the Cu doped sample, compensating V_{Se} defect formation arises due to charge imbalance upon Cu^+ introduction. The local defect introduces additional nonradiative recombination pathways which decrease the EQE with respect to the other samples. Considering the Cu,In sample, increased lattice strain from the large In size relative to Al and Ga suggests that defects are introduced upon In codoping to accommodate lattice distortion. However, and interestingly, the Cu,In sample has the longest lifetime of all the samples studied, vide infra, which implies that the square of the transition dipole moment ($|\mu_{if}|^2$) is highest in this sample. This should translate to increased EQE, however, defect emission present in this sample suggests that alternative pathways for recombination exist apart from the desired DAP ($\text{In}^{2+} + \text{Cu}^{2+} \rightarrow \text{In}^{3+} + \text{Cu}^{+} + h\nu$) channel that result in decreased EQE. While EQE is lower in this sample, the internal QY for this DAP channel is likely much higher, as suggested by the increased radiative lifetime compared to other samples studied. Hence, while EQE is useful for helping gain a better understanding of overall performance efficiencies, the internal QY for the DAP channel of interest is not well represented by these measurements. Additional studies are required to determine if the Cu,In could be further optimized to eliminate these defect channels.

3.5. Increased Lifetime of Photocarriers with Codoping.

To further elucidate the effect of the dopant and codopants on the recombination pathways of photogenerated charge carriers in the ZnSe host lattice, we investigated the time dependence of the PL with time-correlated single photon counting (TCSPC) technique by monitoring the $\lambda_{\max}$ for the Cu-related emission of the doped samples and the $\lambda_{\max}$ for the band edge PL of the undoped sample (Figure 5). The undoped ZnSe/ZnS signal decayed completely within 100 ns, a time frame typical of similar QD core/shell structures.[53] In stark contrast, all of the doped samples exhibited decays which extended for several hundreds of nanoseconds, which is also consistent with previous reports.[54,55] This result indicates that introduction of the dopant significantly stabilizes the photogenerated carriers.

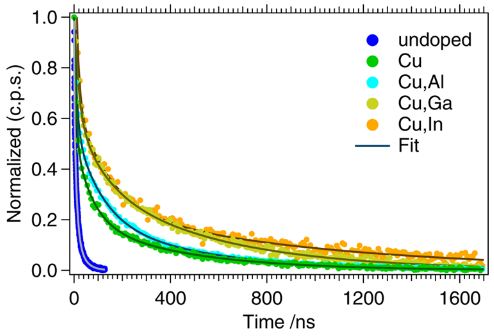

Figure 5. Time-resolved photoluminescence of undoped ZnSe/ZnS (undoped), ZnSe:Cu,Al/ZnS (Cu,Al), ZnSe:Cu/ZnS (Cu), ZnSe:Cu,Ga/ZnS (Cu,Ga), and ZnSe:Cu,In/ZnS (Cu,In). Fit traces are shown superimposed. Spectra were fit with a triple exponential decay; extracted time constants are as follows: undoped (0.9, 9.3, and 30 ns), Cu (7.8, 87, and 470 ns), Cu,Al (7.5, 110, and 480 ns), Cu,Ga (16, 156, and 710 ns), and Cu,In (9.4, 120, and 940 ns). Amplitudes are displayed in SI Table S1.

To extract the lifetimes and gain deeper insight into the fundamental recombination processes from the dynamics traces, we applied a multiexponential fitting procedure to each trace using eq 2 in which τ_i and A_i are the fundamental time constant and initial amplitude of the ith recombination channel, respectively. All samples required a triple exponential fit, and the resultant τ_i and A_i values are listed in SI Table S1; the fits are also shown in Figure 5.

$$I(t) = \sum_{i=1}^{3} A_i e^{-t/\tau_i} \tag{2}$$

For undoped ZnSe, the fitting revealed three components with lifetimes of 0.9 ± 0.1 ns, 9.3 ± 1.4 ns, and 30 ± 4.5 ns. The majority of the recombination occurred through the 9.3 ns pathway and is attributed to band edge recombination.[53] We attribute the slow component (30 ns) to trapped carriers and the fast component (0.9 ns) dominated by nonradiative recombination channels. For the doped samples, the extracted lifetime components were on the order of fast (~10 ns), medium (~100−200 ns), and slow (~600−1000 ns) time scales. Any difference in the fast component of the doped samples was indistinguishable within the error of the measurements. However, the medium lifetime of the doped samples increased in order of Cu < Cu,Al ≈ Cu,In < Cu,Ga and was found to be 87 ± 13 ns, 110 ± 16 ns, 120 ± 18 ns, and 156 ± 23 ns, respectively. Finally, the longest time constant increased in order of Cu = Cu,Al < Cu,Ga < Cu,In, and was found to be 470 ± 70 ns, 480 ± 70 ns, 710 ± 110 ns, and 940 ± 150 ns, respectively. The change in lifetime is attributed to stabilization of photocarriers at the Cu^+ and D^{3+} states within the bandgap.

From previous reports, Cu introduces an acceptor level at ~500−600 meV above the valence band edge due to the t_2 orbitals.[56] Upon excitation of the host lattice, the photogenerated hole will become trapped at this acceptor level, transforming Cu^+ into Cu^{2+} in the excited state and giving it the same oxidation state as the host lattice (Zn^{2+}). This d^9 species has the beneficial effect of stabilizing the photohole, thereby increasing the PL lifetime in the singly doped ZnSe system.

Upon introduction of Al^{3+}, the increase in the medium lifetime component is attributed to elimination of V_{Se} defects. From the PL studies, Al^{3+} does not result in a red shift of the Cu-related PL, indicating it does not introduce an acceptor level below the CBM, similar to the case observed in CdS QDs.[57] Additional stabilization of the excited state species was observed for the case of Ga^{3+} and In^{3+} codopants, evidenced by the increase in the slow time constant for these samples. As both codopants have the effect of red-shifting the PL, we infer that Ga and In introduce donor levels in the bandgap of the host that act to localize and trap the photoelectron thereby forming either Ga^{2+} or In^{2+} in the excited state. The combined effect of photohole and photoelectron stabilization in the Cu,Ga- and Cu,In-doped systems increases the PL lifetime significantly over the Cu and Cu,Al samples. For the Cu-, Cu,Ga-, and Cu,In-codoped QDs, we conclude that the PL is generated through donor−acceptor pair (DAP) recombination of the excited carriers.

3.6. Local Structure of the Primary Dopant.

To gain further understanding of the effect of codoping on the electronic structure of the QDs, we next studied the local lattice structure of the dopant sites. To accomplish this goal, extended X-ray absorption fine structure (EXAFS) was employed as it allows bond distances to be measured at resolutions of 0.1 Å with an accuracy of 0.02 Å with elemental specificity.

The Fourier transformed spectra for the Cu and Zn EXAFS of all samples are shown in Figure 6a. The peaks in the spectrum indicate the average distances of atoms adjacent to the element of interest, as observed up to three neighbors away. Note that a well-known photoelectron phase shift moves the apparent peak positions to a distance ~0.40 Å shorter than the expected value,[58] and the actual distances can be obtained via fitting of the EXAFS data. The relative amplitudes offer information regarding the number of neighboring atoms in each shell and are also strongly coupled with the crystallinity/distance distribution of the local structure surrounding the absorbing atom.

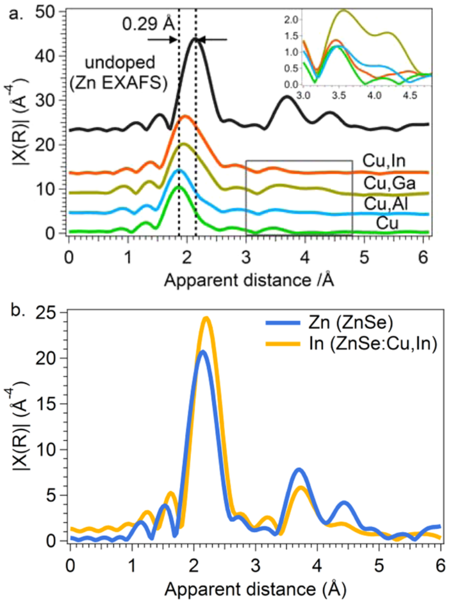

Figure 6. (a) Cu EXAFS indicating the nearest neighbor distances for the probe atom in ZnSe:Cu/ZnS (Cu), ZnSe:Cu,Al/ZnS (Cu,Al), ZnSe:Cu,Ga/ZnS (Cu,Ga), and ZnSe:Cu,In/ZnS (Cu,In) compared to the Zn EXAFS. The inset of panel a shows the expanded region highlighted by the gray box for easier viewing of the second and third neighbor peaks. (b) Zn EXAFS of ZnSe and In EXAFS of ZnSe:Cu,In.

Theoretical EXAFS parameters were calculated starting with cubic ZnSe and replacing the central Zn with Cu. However, in all samples, a Cu−S path has to be included to fit the data, which indicates that some of the Cu is either present on the surface of the ZnSe core or enters the ZnS shell. The latter case is not an unreasonable conclusion considering the synthesis was performed in one pot and residual Cu in the crude pot is likely. The best fits obtained for the first shell using a two-phase system are shown in SI Figure S7 along with the data. The fit results are presented in SI Table S2. As more than one phase existed, leading to multiple shell contributions, a variable parameter x was introduced into the EXAFS equation used by the Artemis program of the IFEFFIT package, shown in eq 3, where x_i is the individual contribution of each phase and $\chi_i(k)$ is the EXAFS function of each individual phase.

$$\chi_{\text{total}}(k) = \sum_i x_i \chi_i(k) \tag{3}$$

Since the roles of x_i and the coordination number (N_j) should be complementary, the coordination number for each phase

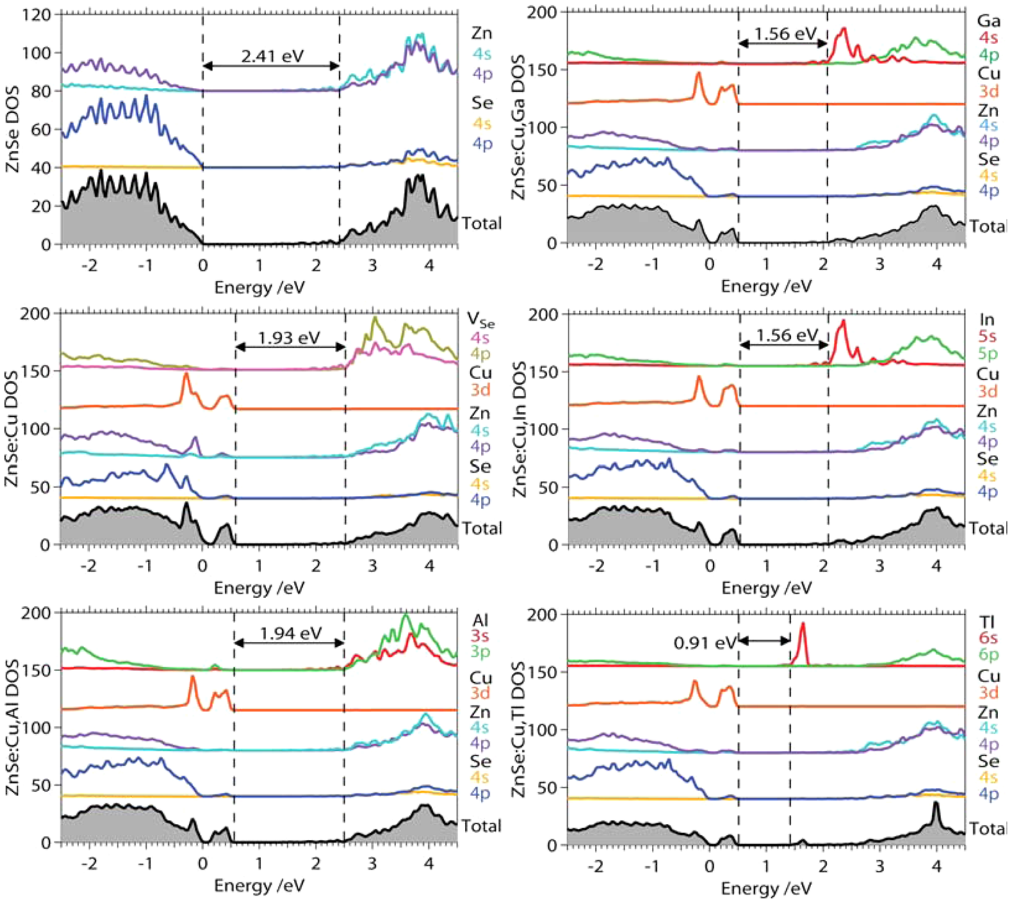

Figure 7. DFT calculations of the PDOS for ZnSe:Cu$^+$,D^{3+} (D = Al, Ga, In, Tl).

was fixed while x was used as a variable parameter during the fitting process.

From the EXAFS data fitting and analysis, we estimate that only ~30% of the Cu$^+$ in the Cu sample has Se nearest neighbors, whereas the remaining Cu has S neighbors. The addition of Al^{3+} as a codopant increased the fraction of Cu$^+$ associated with the ZnSe core to ~50% while addition of Ga^{3+} improved the Cu$^+$ doping to ~60%. The core content was comparable for Cu,In and Cu,Al codoping. The inclusion of D^{3+}, also at a Zn^{2+} site, allows for the addition of a Cu$^+$ atom without creating a selenium vacancy (V$_{Se}$), thereby increasing the solubility in the core. Local structure parameters for In and Cu in the QD samples as determined from the best fits of Fourier transformed data are given in SI Table S2.

In cubic, undoped ZnSe, Zn is tetrahedrally coordinated by four Se atoms which are at a distance of 2.45 Å, and the corresponding peak in the EXAFS data appears at an apparent distance of ~2.1 Å. The second peak at 3.65 Å and third peak at 4.40 Å originate from the 12 Zn second neighbors and 12 Se third neighbors, which are at distances of 4.01 and 4.70 Å, respectively.[28,59] In the Cu sample, the average Cu−Se distance is 2.35 Å, which is 0.1 Å shorter than the Zn−Se bond length (Figure 6a). This is consistent with previous reports indicating that Cu occupies a distorted tetrahedral site after replacing Zn.[28,60−62] A lengthening of the Cu−Se bond distance to 2.37 Å was observed in Cu,Al. This suggests that the environment around Cu is less distorted than the singly doped sample because of elimination of V$_{Se}$ and return of Cu toward a tetrahedral-like geometry. For Cu,Ga, the Cu−Se distance was found to be 2.39 Å, which again is closer to that of a perfect tetrahedral site (2.45 Å). We attribute this effect to smaller lattice distortions due to comparable sizes of Zn, Cu, and Ga. Finally, in Cu,In, the Cu−Se distance was 2.38 Å as a result of the larger In size leading to increased lattice strain.

Further evidence of the change in local structure symmetry can be found from examination of the second and third neighbor amplitudes. For the Cu trace (Figure 6a), the second and third neighbor peaks are absent, whereas for Cu,Al, the second and third neighbor peaks increase in amplitude (more easily seen in the inset of Figure 6a). Likewise, Cu,Ga exhibits an additional increase in these two peaks. On the other hand, the second and third neighbor peaks decrease in amplitude for Cu,In. These results suggest that the size of the codopant strongly affects the degree of disorder around the primary dopant. As previously discussed, doping with only Cu$^+$ results in a lattice charge imbalance which may be compensated through doping with a second Cu$^+$ and creating a V$_{Se}$.[28,61] Considering the second and third neighbor amplitudes, it is evident that the V$_{Se}$ is created adjacent to the Cu dopants. Ga is comparable in size to that of Zn and Cu and thus results in the least disorder around the primary dopant. Furthermore, the effect of the codopant on the local structure of Cu suggests that the codopant occupies a lattice site in the vicinity of the Cu$^+$ dopant. Consequently, the DAP-related recombination described previously occurs through a spatially localized photohole and photoelectron at the acceptor and donor sites.

3.7. Local Structure of the Codopant. EXAFS studies of the Al^{3+} codopant are hampered by Se L_1-edge absorption overlap, and in the case of Ga^{3+}, overwhelming fluorescence signal from Zn makes it impossible to measure the absorption spectrum using fluorescence yield. Consequently, In^{3+} was the only viable option for studying local structure of the codopant. The EXAFS signal for In is shown in Figure 6b, along with that of Zn for comparison. High similarity between the In and Zn EXAFS indicates that In^{3+} occupies a Zn^{2+} substitutional site. However, the first peak for In^{3+} appears at a slightly longer distance as compared to Zn^{2+}. From EXAFS fitting analysis, the In−Se first neighbor distance was longer than that of Zn−Se by 0.10 Å, extending to 2.55 Å instead of 2.45 Å (SI Table S2). The Se atoms are pushed to longer bond distances because of the larger ionic size of In^{3+} compared to Zn^{2+}.

3.8. Density Function Theory Calculations of Cu^+ Doped and D^{3+} Codoped ZnSe.

To further understand the origin of the PL in the codoped ZnSe system as a consequence of doping and codoping, we applied DFT to a 64 atom ZnSe supercell as a model system. The cubic supercell was optimized to obtain a unit cell parameter of $a = 5.67$ Å. In this unit cell, one Zn was replaced with Cu and the bond distances from Cu to three of the nearest Se atoms were fixed to the bond distance determined with EXAFS (Cu−Se = 2.36 Å). A second Zn directly adjacent to the Cu was replaced by the D atom (D = Al, Ga, In, or Tl) in the case of the donor systems. For the ZnSe:Cu system, a second Zn was replaced by a Cu and the shared Se atom was removed to create the V_{Se} necessary for charge neutrality. Compared to our previous report,[28] all lattice ion positions were optimized with the exception of the constraint on the Cu−Se bond distance; DFT modeling was not able to correctly predict the defective Cu−Se bond distance or local geometry of Cu in the ZnSe lattice, which EXAFS reveals is defect trigonal planar, as geometry optimization of the Cu local structure results in a perfect tetrahedral local structure. The codopant, however, as was previously discussed, is tetrahedral in the ZnSe:Cu,In system and therefore by extension should also be tetrahedral for the other codopants. The bond distances to the nearest neighbors vary as a consequence of ion size. The optimized D−Se bond distances were 2.456 Å (Al−Se), 2.481 Å (Ga−Se), and 2.642 Å (In−Se) while the host bond distance was 2.454 Å (Zn−Se).

The partial density of states (PDOS) for all of the systems under investigation are reported in Figure 7. For the host ZnSe system, the predicted E_g was 2.41 eV which is a factor of 0.89 lower than the expected E_g of 2.70 eV. From the PDOS, the VB is primarily Se 2p character hybridized with Zn 4p. The CB is a mixture of both Zn 4p and 4s as a result of sp^3 hybridization in the tetrahedral ligand field. These states are also well-hybridized with Se 2p in the CB.

Doping with Cu introduces two new states, the e and t_2 levels formed from ligand field d orbital splitting. The Cu e states are located within the VB and contribute to the VBM while the t_2 states are observed between 0.16 and 0.56 eV above the VBM. The defective Zn, adjacent to the V_{Se} and having only three Se bonds, is indicated in Figure 7 as V_{Se}. The Zn 4p and 4s orbitals have significantly more DOS toward the CBM compared to bulk Zn and slightly extend into the band gap. This is contrary to our previous report where we observed V_{Se} states within the E_g.[28] These states were removed upon improvements to the computational model by optimizing the local structure around the defect. From the combination of the two results, we can conclude that any deviation from the optimum structure will create additional states within the E_g related to the Zn dangling bonds. These states may become activated by phonons at elevated temperatures or lattice strain. The effects are not taken into account herein but are likely to play a significant role in the V_{Se}-related emission discussed earlier and in our previous report. Finally, the calculated gap related to Cu emission was 1.93 eV.

Doping with both Cu and Al introduces additional DOS from the Al 3s and 3p states. The Al-related states are well-hybridized with the CB and do not extend below the CBM. The 3s states do contribute to more DOS at the CBM relative to the 3p states, as was also the case for Zn. Consequently the E_g was calculated to be 1.94 eV. This result is consistent with the observed PL shift between the Cu and Cu,Al samples, as the Cu,Al is blue-shifted from the Cu sample.

A significant change in the DOS was observed in ZnSe:Cu,Ga as a consequence of Ga. While the Cu states were the same as previously described (t_2 = 0.06 to 0.50 eV above the VBM), a new donor state related to Ga 4s was added at CBM − 0.52 eV. The resulting gap between the Cu and Ga states was calculated to be 1.56 eV. The remaining Ga 4p states remained well-hybridized with the host lattice and mirrored the DOS seen from Zn 4p. This result supports the previously discussed model for DAP emission in this system.

A similar effect was seen in the ZnSe:Cu,In sample; however the predicted bandgap is the same as that of ZnSe:Cu,Ga. This could arise from an inaccurate description of In in the computational model or because the Cu−Se bond distances were held constant during the optimization procedure for these calculations. The acceptor level of Cu is seen to change its energetic level depending on the magnitude of distortion away from perfect tetrahedral. The DOS for ZnSe:Cu,Ga in which the Cu−Se bond distances were not fixed during the optimization is shown in Figure 8. This results in a perfect tetrahedral symmetry for Cu. Consequently, the predicted E_g moved to 1.50 eV for the perfect tetrahedron (longer Cu−Se bond distances) from 1.56 eV for Cu in the distorted site (shorter Cu−Se bond distances). The red shift in the ZnSe:Cu,In PL, as compared to that of ZnSe:Cu,Ga, is likely

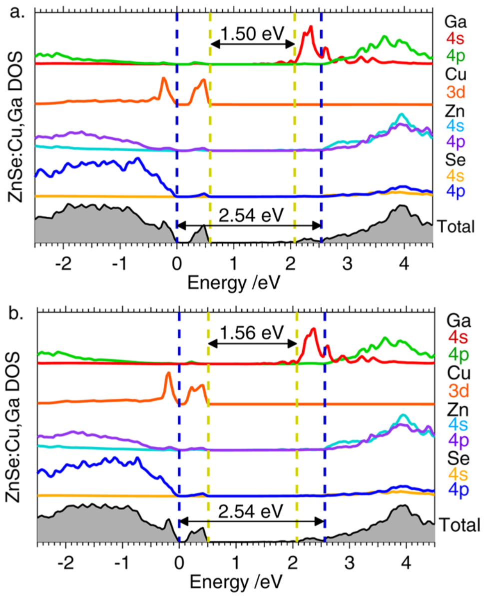

Figure 8. Density of states of ZnSe:Cu,Ga QDs (a) in which both Cu and Ga are in perfect tetrahedral sites whereas b has Cu in the distorted tetrahedral site, as expected from the EXAFS analysis.

a contribution from the slight change in the Cu local structure toward a more tetrahedral structure in the Cu,In system, which is consistent with the EXAFS analysis.

Finally, ZnSe:Cu,Tl (Cu,Tl) was studied as a potential candidate for red emission in this system. While attempts were made to produce the Cu,Tl variant, the large size of Tl is particularly challenging to incorporate and contributed to significant distortion to the host lattice. The PL of an example Cu,Tl sample is shown in SI Figure S4 which demonstrates an emission maximum at approximately 635 nm. The significant host emission is indicative of incomplete doping, and the significant broadening and multiple component emission in the red suggests inhomogeneous Tl^{3+}-related electronic states. When the ZnSe:Cu,Tl core was modeled, the PDOS related to Cu remained the same as previously described; however, the donor state from Tl 6s moved to CBM − 1.2 eV and extended up to CBM − 0.84 eV. The resulting DAP recombination in this system is calculated to be 0.91 eV. For Tl →VBM 4s emission, the calculated transition would be 1.4 eV.

3.9. Energetic Model of Cu^+ Doped and D^{3+} Codoped ZnSe. The energy levels of the donor and acceptor states described earlier, as well as the lifetimes for the various recombination channels, are summarized in the energy level model shown in Figure 9a. The observed bandgap from UV−vis is indicated (2.97 eV) as well as the band edge PL (437 nm). The energy levels of the dopant and codopants are provided with respect to either the VB or CB, respectively. The $\pm\delta$ shown in Figure 9a accounts for variation of the Cu level as a function of local structure distortions caused by the codopant, as previously discussed. The extent of tunability of these systems by quantum confinement has not been fully examined by us at this point; however, the Cu^+-related emission in Cu:ZnSe has proven to be tunable through quantum confinement of the host, allowing for an additional parameter to modify the emission.[63]

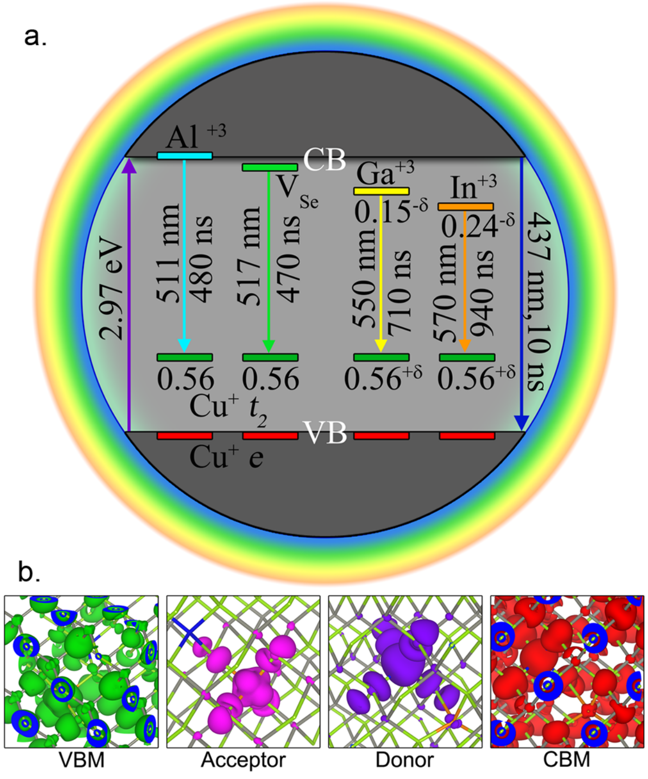

Figure 9. (a) Summary of the electronic energy levels and fluorescence lifetimes of ZnSe doped with Cu^+ and codoped with Al^{3+}, Ga^{3+}, or In^{3+}. (b) Integrated local DOS showing the spatial occupation of the DOS for the VBM, Cu-related acceptor state, Ga-related donor state, and the CBM.

As a visualization aid for the states of interest, the integrated local DOS for the VBM, CBM, Cu-related acceptor, and codopant donor level for Ga (the In ILDOS are very similar to the Ga orbital shape) are shown in Figure 9b. Here it is easy to see the spatial extent of charge localization on the donor and acceptor states, thereby improving the initial and final state wave function overlap that is critical for efficient PL with high yield.

4. CONCLUSION

We have synthesized novel codoped, ligand-capped, core/shell ZnSe/ZnS QDs with PL tunable from blue to orange and characterized in detail their morphological, optical, dynamic, and structural properties. In single doping, Cu dopes the ZnSe lattice as a +1 ion at a Zn site, resulting in a lattice charge imbalance that is compensated for by the formation of Se vacancies. Utilization of a trivalent cation (D^{3+}) as a codopant reduces defect formation by neutralizing the charge imbalance from the initial Cu^+ doping and consequently improves the PL EQE. The codopant also introduces a donor state into the ZnSe bandgap, whose energy level can be lowered further from the CB by changing the codopant from Al to Ga and In. The combination of these effects allows for tunable emission from ZnSe QDs throughout the visible region of the spectrum. The introduction of Cu has the effect of increasing the photohole lifetime compared to the undoped system, whereas Ga and In codopants stabilize the photoelectron lifetime, by localizing the carriers in midgap states. In addition, through incorporation of a ZnS shell in conjunction with a modified lipoic acid capping ligand, QD stability to postsynthetic processing and long-term storage was substantially improved, and PL was enhanced by about 1 order of magnitude. Furthermore, EXAFS analysis elucidated the local structure of both the primary Cu^+ dopant and In^{3+} codopant, indicating that they occupy a distorted trigonal planar and tetrahedral substitutional Zn site, respectively. The dopant and codopants were seen to occupy neighboring lattice positions which results in increased wave function overlap for improved PL emission. Computational studies provide further insight into the electronic states involved and their related energy levels as well as correlation to structural properties. Our codoped ZnSe/ZnS QD system represents an efficient and economical alternative to conventional CdSe lighting materials and should reduce the use of toxic Cd while still offering improved chromophoric quality of display devices through tunable emission with limited self-absorption.

■ ASSOCIATED CONTENT

Ⓢ Supporting Information

Additional discussion and details regarding QD and capping ligand synthesis, capping ligand effects on the PL, PL Gaussian fitting results, EELS spectra taken of the core and shell regions of a ZnSe/ZnS QD, EXAFS analysis, EXAFS fitting parameters and traces, and DFT calculation results including DOS. The Supporting Information is available free of charge on the ACS Publications website at DOI: 10.1021/acsami.5b02860.

AUTHOR INFORMATION

Corresponding Author

*E-mail: zhang@ucsc.edu.

Notes

The authors declare no competing financial interest.

ACKNOWLEDGMENTS

Special thanks to Drs. Adam Schwartzberg, Ian Sharp, and Francesca Toma for their insightful discussions. We acknowledge the Joint Center for Artificial Photosynthesis (JCAP) for access to temperature dependent PL equipment. This project was funded by the U.S. Department of Energy under Contract No. DE-FG02-07ER46388-A002. For the use of the HRTEM facilities, we are grateful to Dr. Chengyu Song and the authorities at National Center for Electron Microscopy, Lawrence Berkeley National Laboratory, which is supported by the U.S. Department of Energy under Contract No. DE-AC02-05CH11231. XAS work was funded by the Director, Office of Science, Office of Basic Energy Sciences (OBES), Division of Chemical Sciences, Geosciences, and Biosciences of the Department of Energy (DOE) under Contract No. DE-AC02-05CH11231 (J.Y.) and carried out at the Stanford Synchrotron Radiation Light source BL 7-3, a Directorate of SLAC National Accelerator Laboratory and an Office of Science User Facility operated for the U.S. Department of Energy Office of Science by Stanford University. DFT calculations were performed on the UCSC campusrocks cluster.

REFERENCES

(1) Resch-Genger, U.; Grabolle, M.; Cavaliere-Jaricot, S.; Nitschke, R.; Nann, T. Quantum Dots Versus Organic Dyes as Fluorescent Labels. *Nat. Methods* **2008**, *5*, 763−775.

(2) Chen, C.-C.; Herhold, A. B.; Johnson, C. S.; Alivisatos, A. P. Size Dependence of Structural Metastability in Semiconductor Nanocrystals. *Science* **1997**, *276*, 398−401.

(3) Murray, C. B.; Norris, D. J.; Bawendi, M. G. Synthesis and Characterization of Nearly Monodisperse CdE (E = Sulfur, Selenium, Tellurium) Semiconductor Nanocrystallites. *J. Am. Chem. Soc.* **1993**, *115*, 8706−8715.

(4) Alivisatos, A. P. Semiconductor Clusters, Nanocrystals, and Quantum Dots. *Science* **1996**, *271*, 933−937.

(5) Burda, C.; Chen, X.; Narayanan, R.; El-Sayed, M. A. Chemistry and Properties of Nanocrystals of Different Shapes. *Chem. Rev.* **2005**, *105*, 1025−1102.

(6) Wang, Y.; Herron, N.; M?ller, K.; Bein, T. Three-Dimensionally Confined Diluted Magnetic Semiconductor Clusters: $Zn_{1-x}Mn_xS$. *Solid State Commun.* **1991**, *77*, 33−38.

(7) Chen, W.; Zhang, J. Z.; Joly, A. G. Optical Properties and Potential Applications of Doped Semiconductor Nanoparticles. *J. Nanosci. Nanotechnol.* **2004**, *4*, 919−947.

(8) Erwin, S. C.; Zu, L.; Haftel, M. I.; Efros, A. L.; Kennedy, T. A.; Norris, D. J. Doping Semiconductor Nanocrystals. *Nature* **2005**, *436*, 91−94.

(9) Wood, V.; Bulović, V. Colloidal Quantum Dot Light-Emitting Devices. *Nano Rev.* **2010**, *1*, 1−7.

(10) Jun, S.; Lee, J.; Jang, E. Highly Luminescent and Photostable Quantum Dot−Silica Monolith and Its Application to Light-Emitting Diodes. *ACS Nano* **2013**, *7*, 1472−1477.

(11) Bowers, M. J.; McBride, J. R.; Rosenthal, S. J. White-Light Emission from Magic-Sized Cadmium Selenide Nanocrystals. *J. Am. Chem. Soc.* **2005**, *127*, 15378−15379.

(12) Colvin, V. L.; Schlamp, M. C.; Alivisatos, A. P. Light-Emitting Diodes Made From Cadmium Selenide Nanocrystals and a Semiconducting Polymer. *Nature* **1994**, *370*, 354−357.

(13) Schlamp, M.; Peng, X.; Alivisatos, A. Improved Efficiencies in Light Emitting Diodes Made with CdSe (CdS) Core/Shell Type Nanocrystals and a Semiconducting Polymer. *J. Appl. Phys.* **1997**, *82*, 5837−5842.

(14) Zhao, J.; Bardecker, J. A.; Munro, A. M.; Liu, M. S.; Niu, Y.; Ding, I.-K.; Luo, J.; Chen, B.; Jen, A. K.-Y.; Ginger, D. S. Efficient CdSe/CdS Quantum Dot Light-Emitting Diodes Using a Thermally Polymerized Hole Transport Layer. *Nano Lett.* **2006**, *6*, 463−467.

(15) Sun, Q.; Wang, Y. A.; Li, L. S.; Wang, D.; Zhu, T.; Xu, J.; Yang, C.; Li, Y. Bright, Multicoloured Light-Emitting Diodes Based on Quantum Dots. *Nat. Photonics* **2007**, *1*, 717−722.

(16) Anikeeva, P. O.; Halpert, J. E.; Bawendi, M. G.; Bulovic, V. Quantum Dot Light-Emitting Devices with Electroluminescence Tunable Over the Entire Visible Spectrum. *Nano Lett.* **2009**, *9*, 2532−2536.

(17) Qian, L.; Zheng, Y.; Xue, J.; Holloway, P. H. Stable and Efficient Quantum-Dot Light-Emitting Diodes Based on Solution-Processed Multilayer Structures. *Nat. Photonics* **2011**, *5*, 543−548.

(18) Kwak, J.; Bae, W. K.; Lee, D.; Park, I.; Lim, J.; Park, M.; Cho, H.; Woo, H.; Yoon, D. Y.; Char, K. Bright and Efficient Full-Color Colloidal Quantum Dot Light-Emitting Diodes Using an Inverted Device Structure. *Nano Lett.* **2012**, *12*, 2362−2366.

(19) Pradhan, N.; Sarma, D. D. Advances in Light-Emitting Doped Semiconductor Nanocrystals. *J. Phys. Chem. Lett.* **2011**, *2*, 2818−2826.

(20) Mueller, A. H.; Petruska, M. A.; Achermann, M.; Werder, D. J.; Akhadov, E. A.; Koleske, D. D.; Hoffbauer, M. A.; Klimov, V. I. Multicolor Light-Emitting Diodes Based on Semiconductor Nanocrystals Encapsulated in GaN Charge Injection Layers. *Nano Lett.* **2005**, *5*, 1039−1044.

(21) Godt, J.; Scheidig, F.; Grosse-Siestrup, C.; Esche, V.; Brandenburg, P.; Reich, A.; Groneberg, D. A. The Toxicity of Cadmium and Resulting Hazards for Human Health. *J. Occup. Med. Toxicol. (London, U. K.)* **2006**, *1*, 1−6.

(22) Karan, N. S.; Sarma, D. D.; Kadam, R. M.; Pradhan, N. Doping Transition Metal (Mn or Cu) Ions in Semiconductor Nanocrystals. *J. Phys. Chem. Lett.* **2010**, *1*, 2863−2866.

(23) Pawlikowski, J. M. Absorptivity and Photoluminescence of Compensated ZnSe:Ga. *Solid State Commun.* **1985**, *55*, 31−33.

(24) Norris, D. J.; Efros, A. L.; Erwin, S. C. Doped Nanocrystals. *Science* **2008**, *319*, 1776−1779.

(25) Sharma, V. K.; Guzelturk, B.; Erdem, T.; Kelestemur, Y.; Demir, H. V. Tunable White-Light-Emitting Mn-Doped ZnSe Nanocrystals. *ACS Appl. Mater. Interfaces* **2014**, *6*, 3654−3660.

(26) Pradhan, N.; Goorskey, D.; Thessing, J.; Peng, X. An Alternative of CdSe Nanocrystal Emitters: Pure and Tunable Impurity Emissions in ZnSe Nanocrystals. *J. Am. Chem. Soc.* **2005**, *127*, 17586−17587.

(27) Wu, P.; Yan, X.-P. Doped Quantum Dots for Chemo/Biosensing and Bioimaging. *Chem. Soc. Rev.* **2013**, *42*, 5489−5521.

(28) Gul, S.; Cooper, J. K.; Glans, P.-A.; Guo, J.; Yachandra, V. K.; Yano, J.; Zhang, J. Z. Effect of Al^{3+} Co-Doping on the Dopant Local Structure, Optical Properties, and Exciton Dynamics in Cu^+-Doped ZnSe Nanocrystals. *ACS Nano* **2013**, *7*, 8680−8692.

(29) Allen, J. Spectroscopy of Lattice Defects in Tetrahedral II-VI Compounds. *Semicond. Sci. Technol.* **1995**, *10*, 1049−1064.

(30) Kennedy, T.; Glaser, E.; Murdin, B.; Pidgeon, C.; Prior, K.; Cavenett, B. Identification of V_{Se}-Impurity Pairs in ZnSe:N. *Appl. Phys. Lett.* **1994**, *65*, 1112−1114.

(31) Corrado, C.; Cooper, J. K.; Hawker, M.; Hensel, J.; Livingston, G.; Gul, S.; Vollbrecht, B.; Bridges, F.; Zhang, J. Z. Synthesis and Characterization of Organically Soluble Cu-Doped ZnS Nanocrystals With Br Co-Activator. *J. Phys. Chem. C* **2011**, *115*, 14559−14570.

(32) Manzoor, K.; Vadera, S.; Kumar, N.; Kutty, T. Synthesis and Photoluminescent Properties of ZnS Nanocrystals Doped with Copper and Halogen. *Mater. Chem. Phys.* **2003**, *82*, 718−725.

(33) Manzoor, K.; Vadera, S. R.; Kumar, N.; Kutty, T. R. N. Multicolor electroluminescent devices using doped ZnS nanocrystals. *Appl. Phys. Lett.* **2009**, *84*, 284−286.

(34) Zhang, J. Z.; Cooper, J. K.; Gul, S. Rational Codoping as a Strategy to Improve Optical Properties of Doped Semiconductor Quantum Dots. *J. Phys. Chem. Lett.* **2014**, *5*, 3694−3700.

(35) Gul, S.; Cooper, J. K.; Corrado, C.; Vollbrecht, B.; Bridges, F.; Guo, J.; Zhang, J. Z. Synthesis, Optical and Structural Properties, and Charge Carrier Dynamics of Cu-Doped ZnSe Nanocrystals. *J. Phys. Chem. C* **2011**, *115*, 20864−20875.

(36) Giannozzi, P.; Baroni, S.; Bonini, N.; Calandra, M.; Car, R.; Cavazzoni, C.; Ceresoli, D.; Chiarotti, G. L.; Cococcioni, M.; Dabo, I.; et al. QUANTUM ESPRESSO: A Modular and Open-Source Software Project for Quantum Simulations of Materials. *J. Phys.: Condens. Matter* **2009**, *21*, No. 395502.

(37) Newville, M. IFEFFIT: Interactive XAFS Analysis and FEFF Fitting. *J. Synchrotron Radiat.* **2001**, *8*, 322−324.

(38) Ravel, Á.; Newville, M. ATHENA, ARTEMIS, HEPHAESTUS: Data Analysis for X-ray Absorption Spectroscopy Using IFEFFIT. *J. Synchrotron Radiat.* **2005**, *12*, 537−541.

(39) Zabinsky, S.; Rehr, J.; Ankudinov, A.; Albers, R.; Eller, M. Multiple-Scattering Calculations of X-ray-Absorption Spectra. *Phys. Rev. B* **1995**, *52*, 2995−3009.

(40) Jana, S.; Srivastava, B. B.; Acharya, S.; Santra, P. K.; Jana, N. R.; Sarma, D.; Pradhan, N. Prevention of Photooxidation in Blue−Green Emitting Cu Doped ZnSe Nanocrystals. *Chem. Commun. (Cambridge, U. K.)* **2010**, *46*, 2853−2855.

(41) Dabbousi, B. O.; Rodriguez-Viejo, J.; Mikulec, F. V.; Heine, J. R.; Mattoussi, H.; Ober, R.; Jensen, K. F.; Bawendi, M. G. (CdSe)ZnS Core−Shell Quantum Dots: Synthesis and Characterization of a Size Series of Highly Luminescent Nanocrystallites. *J. Phys. Chem. B* **1997**, *101*, 9463−9475.

(42) Fitzmorris, B. C.; Cooper, J. K.; Edberg, J.; Gul, S.; Guo, J.; Zhang, J. Z. Synthesis and Structural, Optical, and Dynamic Properties of Core/Shell/Shell CdSe/ZnSe/ZnS Quantum Dots. *J. Phys. Chem. C* **2012**, *116*, 25065−25073.

(43) Mikulec, F. V.; Kuno, M.; Bennati, M.; Hall, D. A.; Griffin, R. G.; Bawendi, M. G. Organometallic Synthesis and Spectroscopic Characterization of Manganese-Doped CdSe Nanocrystals. *J. Am. Chem. Soc.* **2000**, *122*, 2532−2540.

(44) Du, M.-H.; Erwin, S. C.; Efros, A. L. Trapped-Dopant Model of Doping in Semiconductor Nanocrystals. *Nano Lett.* **2008**, *8*, 2878−2882.

(45) Bhargava, R. N. Doped Nanocrystalline Materials—Physics and Applications. *J. Lumin.* **1996**, *70*, 85−94.

(46) Ramanathan, S.; Patibandla, S.; Bandyopadhyay, S.; Anderson, J.; Edwards, J. D. Fluorescence Spectroscopy of Electrochemically Self-Assembled ZnSe and Mn:ZnSe Nanowires. *Nanotechnology* **2008**, *19*, No. 195601.

(47) Pelant, I.; Valenta, J. *Luminescence spectroscopy of semiconductors*; Oxford University Press: New York, 2012.

(48) Gutowski, J.; Sebald, K.; Voss, T. In *Landolt-Börnstein III/44B: Semiconductors—New Data and Updates for II−VI Compounds*, Vol. *44*; Springer: Berlin, 2009; pp 304−305.

(49) Nordlund, T. M. *Quantitative Understanding of Biosystems: An Introduction to Biophysics*; CRC Press: Boca Raton, FL, USA, 2011.

(50) O'Donnell, K. P.; Chen, X. Temperature Dependence of Semiconductor Band Gaps. *Appl. Phys. Lett.* **1991**, *58*, 2924−2926.

(51) Murov, S. L.; Carmichael, I.; Hug, G. L. *Handbook of photochemistry*, 2nd ed.; Marcel Dekker: New York, 1993.

(52) Tran, T.-T. D.; Sun, H.; Ng, K. W.; Ren, F.; Li, K.; Lu, F.; Yablonovitch, E.; Chang-Hasnain, C. J. High Brightness InP Micropillars Grown on Silicon with Fermi Level Splitting Larger than 1 eV. *Nano Lett.* **2014**, *14*, 3235−3240.

(53) Fitzmorris, B. C.; Pu, Y.-C.; Cooper, J. K.; Lin, Y.-F.; Hsu, Y.-J.; Li, Y.; Zhang, J. Z. Optical Properties and Exciton Dynamics of Alloyed Core/Shell/Shell $Cd_{1-x}Zn_xSe$/ZnSe/ZnS Quantum Dots. *ACS Appl. Mater. Interfaces* **2013**, *5*, 2893−2900.

(54) Panda, S. K.; Hickey, S. G.; Demir, H. V.; Eychmüller, A. Bright White-Light Emitting Manganese and Copper Co-Doped ZnSe Quantum Dots. *Angew. Chem.* **2011**, *123*, 4524−4528.

(55) Suyver, J.; Van der Beek, T.; Wuister, S.; Kelly, J.; Meijerink, A. Luminescence of Nanocrystalline ZnSe: Cu. *Appl. Phys. Lett.* **2001**, *79*, 4222−4224.

(56) Srivastava, B. B.; Jana, S.; Pradhan, N. Doping Cu in Semiconductor Nanocrystals: Some Old and Some New Physical Insights. *J. Am. Chem. Soc.* **2011**, *133*, 1007−1015.

(57) Ishizumi, A.; Kanemitsu, Y. Photoluminescence Spectra and Dynamics of Al^{3+} and Ag^{+}-Doped CdS Nanocrystals. *J. Phys. Soc. Jpn.* **2010**, *79*, No. 093706.

(58) Teo, B. K. *EXAFS: Basic Principles and Data Analysis*, Vol. *9*; Springer-Verlag: Berlin, 1986.

(59) Norman, T. J.; Magana, D.; Wilson, T.; Burns, C.; Zhang, J. Z.; Cao, D.; Bridges, F. Optical and Surface Structural Properties of Mn^{2+}-Doped ZnSe Nanoparticles. *J. Phys. Chem. B* **2003**, *107*, 6309−6317.

(60) Goldman, A.; Canova, E.; Kao, Y.; Fitzpatrick, B.; Bhargava, R.; Phillips, J. C. Extended X-Ray Absorption Fine Structure Studies of Diffused Copper Impurities in ZnSe. *Appl. Phys. Lett.* **1983**, *43*, 836−838.

(61) Car, B.; Medling, S.; Corrado, C.; Bridges, F.; Zhang, J. Z. Probing the Local Structure of Dilute Cu Dopants in Fluorescent ZnS Nanocrystals Using EXAFS. *Nanoscale* **2011**, *3*, 4182−4189.

(62) Corrado, C.; Jiang, Y.; Oba, F.; Kozina, M.; Bridges, F.; Zhang, J. Z. Synthesis, Structural, and Optical Properties of Stable ZnS: Cu, Cl Nanocrystals. *J. Phys. Chem. A* **2009**, *113*, 3830−3839.

(63) Pradhan, N.; Goorskey, D.; Thessing, J.; Peng, X. An Alternative of CdSe Nanocrystal Emitters: Pure and Tunable Impurity Emissions in ZnSe Nanocrystals. *J. Am. Chem. Soc.* **2005**, *127*, 17586−17587.